Electronic Supplementary Information

Rational Design of Dimensional Matched 2D/2D COFs Based Photocatalysts for Highly Efficient Noble-Metal-Free Solar Energy Catalysis

Haijun Hu[a], Xiaodong Sun*[a], Hui Li[b], Hongwei Huang[c], Tianyi Ma*[b]

[a] *Institute of Clean Energy Chemistry, Key Laboratory for Green Synthesis and Preparative Chemistry of Advanced Materials, College of Chemistry, Liaoning University, Shenyang 110036, People's Republic of China*

[b] *School of Science, RMIT University, Melbourne, VIC 3000, Australia*

[c] *Beijing Key Laboratory of Materials Utilization of Nonmetallic Minerals and Solid Wastes, National Laboratory of Mineral Materials, School of Materials Science and Technology, China University of Geosciences, Beijing, 100083, China*

*Corresponding author.
E-mail address: sunxiaodong@lnu.edu.cn; tianyi.ma@rmit.edu.au.

Keywords: Covalent organic frameworks; Co-catalysts; Photocatalysis; Hydrogen evolution

1. Characterization

SEM images were acquired using a Hitachi SU-8010 equipped with an EDS analyzer. TEM and HRTEM images were obtained on a JEM-2100 operating at 10 kV. XRD patterns were collected using a D8 Advance (Bruker) X-ray diffraction system with a Cu Kα radiation (λ = 0.15406 nm). XPS spectra were recorded by the Thermo Scientific ESCALAB 250Xi spectrometer equipped with a monochromatic Al Kα X-ray source (1486.6 eV). The UV-vis spectra were obtained by the Ultraviolet-visible diffuse reflectance spectroscopy (UV-vis DRS) with $BaSO_4$ as the reflectance standard (Shimadzu UV-2550). Thermogravimetric analysis (TGA, METTLER TOLEDO TGA/SDTA851) was performed to analyze the structure of as-prepared samples with a heating rate of 10 °C·min^{-1} under N_2 atmosphere. The surface area and pore size of prepared samples was investigated by nitrogen adsorption-desorption measurements (QuantaAutosorb IQ). Fluorescence measurements were carried out with the RF-5301PC (Shimadzu, Japan) fluorescence spectrophotometer (excitation wavelength: 350 nm). The Fourier transformed infrared spectroscopy (FT-IR) was performed on a Nicolet Nexus 670 FT-IR spectrophotometer at a resolution of 4 cm^{-1}.

2. Photocatalytic H_2 production properties

Photocatalytic H_2 production experiments were carried out via a full glass automatic on-line trace gas analysis system (Labsolar-6A, Beijing Perfectlight Technology Co., Ltd.). The light source is the 300 W Xenon lamp (wavelength: 320-780 nm, PLS-SXE300/300UV, light intensity: 100 mW·cm^{-2}, Beijing Perfectlight Technology Co., Ltd.). Hydrogen was detected and quantitative analyzed by a GC7900 gas

chromatography (Shanghai Tianmei Scientific Instrument Co.) with nitrogen as the carrier gas, and the detection interval was 30 min. The catalyst was placed in a custom-made quartz glass reactor, and the reaction temperature was controlled at 5 °C by condensing water. 10 mg of catalyst was added into 100 mL of deionized water containing 100 mg of L-Ascorbic acid as hole scavenger. Then, the chloroplatinic acid solution ($H_2PtCl_6 \cdot 6H_2O$) was added. After that, the suspension was stirred in a 200 mL customized quartz reactor. Before each photocatalytic reaction, the system was vacuum-treated several times to remove the dissolved air. The whole reaction system was illuminated by the Xe light irradiation with a UV cut-off filter ($\lambda \geq 420$ nm). In addition, the apparent quantum efficiency (AQE) was measured utilizing a xenon lamp equipped with bandpass filters. Photocatalytic experiments were conducted with 10 mg of catalysts, where the wavelengths of the filters used are 400, 420, 500, 550 and 600 nm, respectively. The specific value of AQE was calculated on the basis of the following formula:

$$AQE(H_2)\% = \frac{2 \times N(H_2)}{N(photons)} \times 100\%$$

where $N(H_2)$ refers to the number of H_2 molecules produced, and N(photons) means the number of photons reaching the surface of the reaction suspension.[1]

3. Photo-electrochemical characterization

The electrochemical measurement was carried out by the electrochemical workstation with the model of CHI 760. The test was carried out in a three-electrode system, in which the Pt sheet was used as the counter electrode, the Ag/AgCl electrode was used as the reference electrode, and the prepared powder sample was used as the working

electrode. In addition, 0.2 M Na_2SO_4 was utilized as the electrolyte solution, and a xenon lamp equipped with a filter ($\lambda \geq 420$ nm) was utilized as the visible light source. 10 mg of catalyst sample and 20 μl of Nafion solution were dissolved in 1 mL of anhydrous ethanol solution, sonicated for 30 min to make them evenly mixed, and then scraped onto FTO glass (1 cm × 1 cm) to manufacture the working electrode. In addition, the Mott-Schottky tests were conducted to acquire the flat-band potential of the material. In the absence of light, the stable open-circuit voltage of this sample was initially measured, and subsequently tested at varying frequencies (500 and 1000 Hz). On the basis of Mott-Schottky equation:

$$\frac{1}{C^2} = \frac{2}{N_D e \varepsilon_0 \varepsilon}(E - E_{fb} - \frac{kT}{e})$$

where C refers to the capacitance of the space charge region, N_D stands for the electron carrier density, e is the elemental charge, ε_0 is the permittivity of a vacuum, ε represents the relative permittivity of the semiconductor, E is the applied potential, E_{fb} is the flat band potential, T is the temperature, and k is the Boltzmann constant. The type of semiconductor material is determined by the positive or negative value of the slope of the linear part of the Mott-Schottky curve: Typically, n-type semiconductors possess a positive slope, while p-type semiconductors have a negative slope.[2]

In addition, the mean lifespan of the photogenerated carriers determined through the open-circuit voltage decay technique is obtained from equation blow:

$$\tau_n = \frac{K_B T}{e}\left(\frac{dOCVD}{dt}\right)^{-1}$$

where K_B stands for the Boltzmann constant, and the value is 1.38×10^{-23} $J\cdot K^{-1}$, T refers to temperature (298 K), e means the electric charge (1.602×10^{-19} C), and dOCVD/dt denotes the derivative of the OCP transient decay.[3]

Fig. S1. Photocatalytic experimental equipment. The labsolar-6a all-glass automatic on-line trace gas analysis system, produced by Beijing Perfectlight Technology Co., Ltd., was utilized for conducting the photocatalytic experiments. The illumination was provided by the 300 W Xenon lamp manufactured by Beijing Perfectlight Technology Co., Ltd. Hydrogen was detected and quantitative analyzed by a GC7900 gas chromatography made by Shanghai Tianmei Scientific Instrument Co.

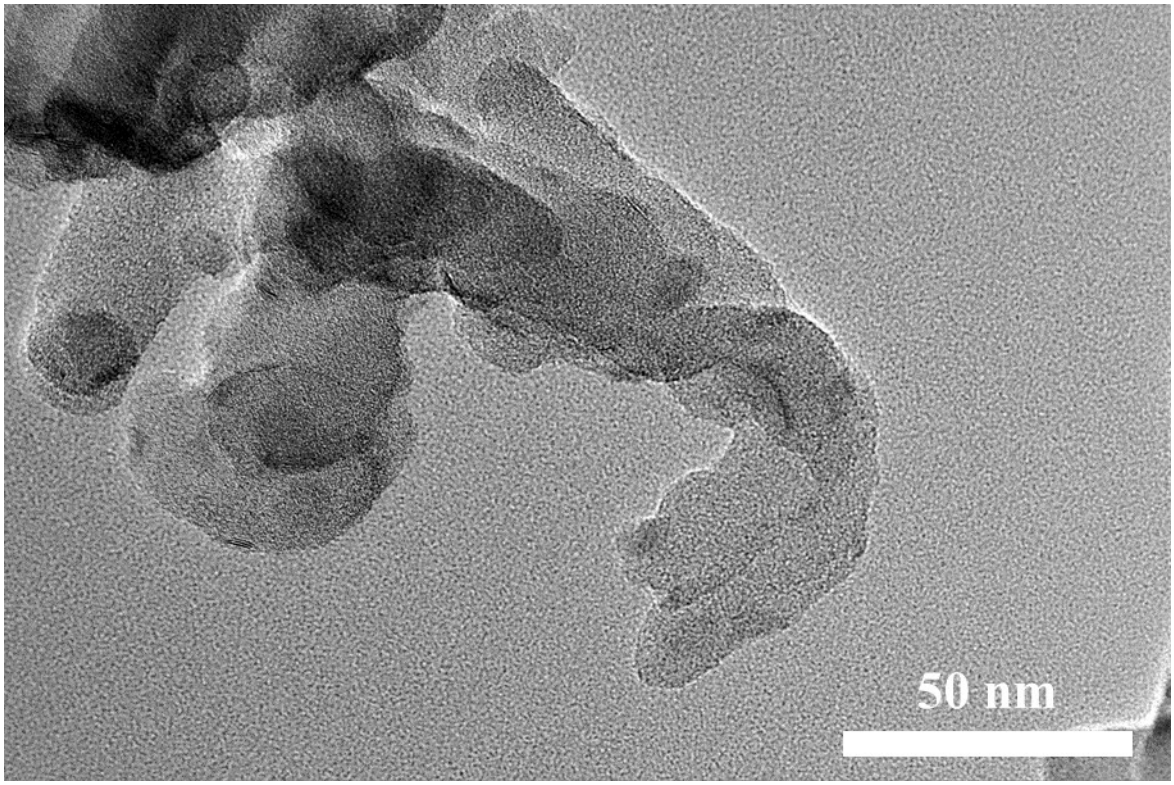

Fig. S2. The TEM image of TP1C. As shown in Fig. S2, TP1C displayed flower-like morphology, which corresponded well with the SEM images.

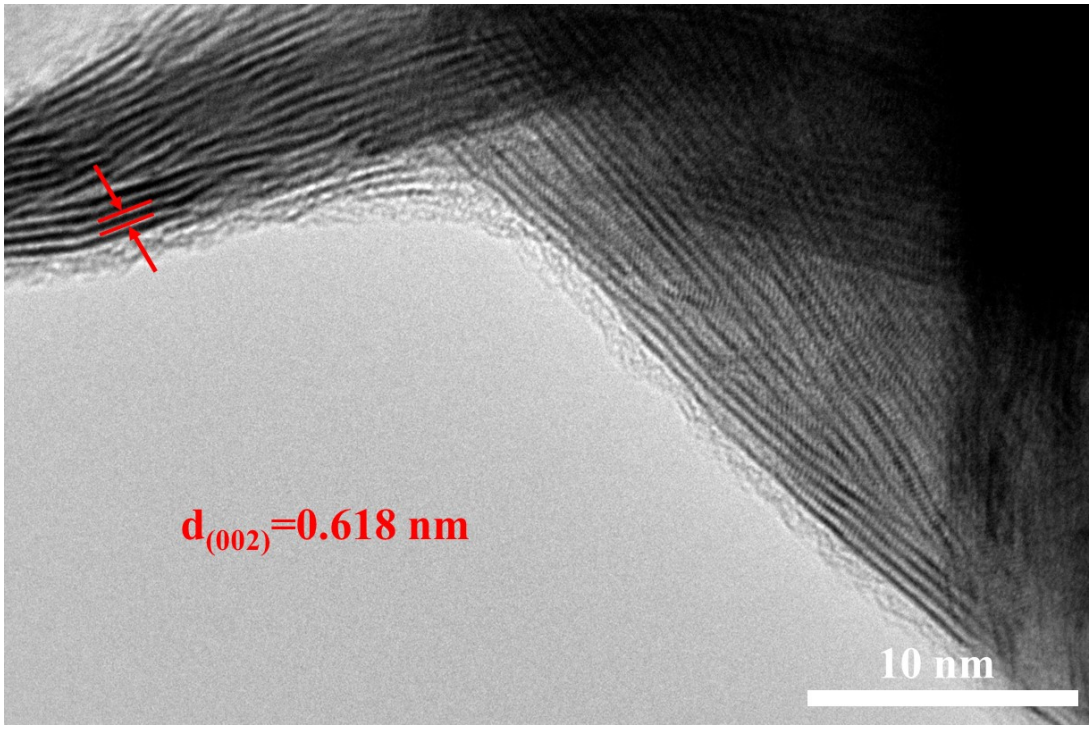

Fig. S3. The HR-TEM images of WS_2. As portrayed in Fig. S3, the lattice spacing of WS_2 was about 0.618 nm, which referred to the (002) crystal plane of WS_2.

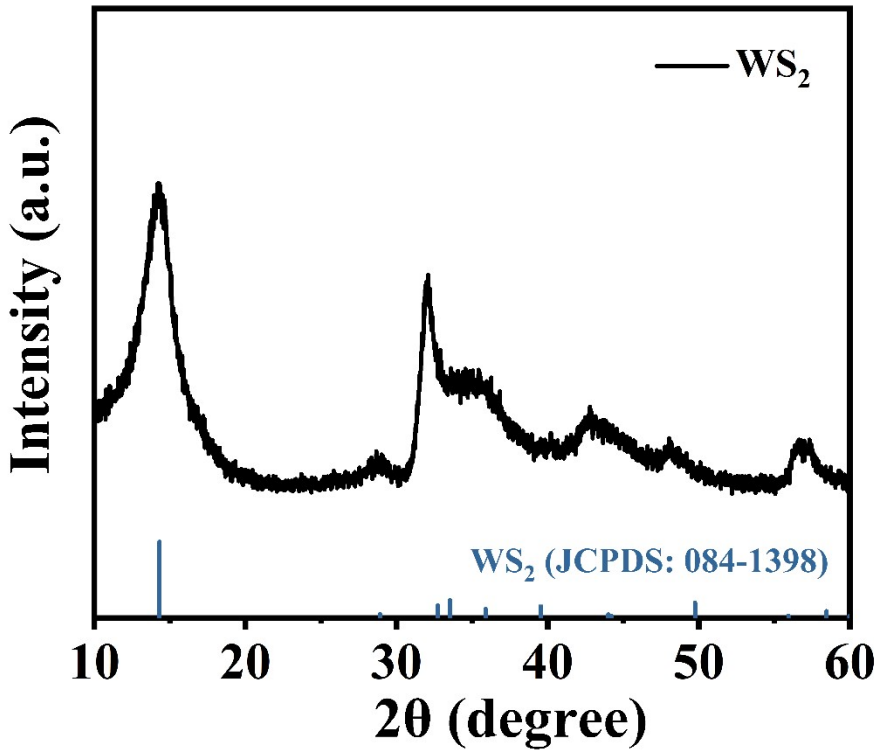

Fig. S4. The XRD spectra of WS_2. It can be seen from Fig.S4 that the peak positions of WS_2 were consistent with JPCDS card (084-1398) for pure hexagonal WS_2, which proved the successful preparation of WS_2 nanosheets.

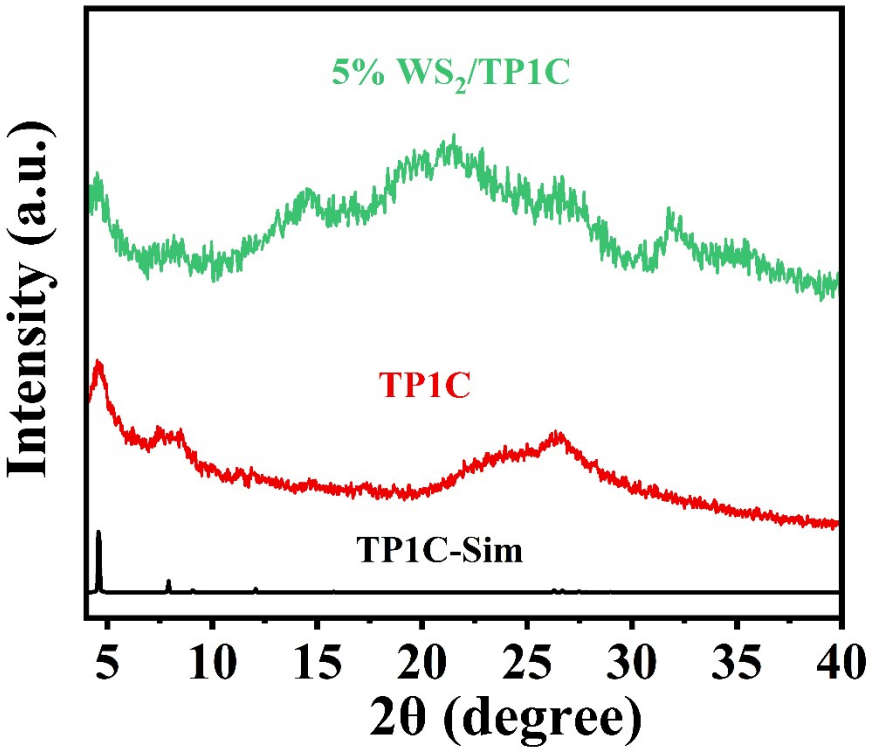

Fig. S5. The XRD spectra of TP1C and 5% WS_2/TP1C. As illustrated in Fig. S5, the diffraction peak positions of the Powder X-ray diffraction (PXRD) tests of TP1C closely matched those of the simulated standard card, with no additional impurity peaks detected, in which the two obvious peaks at 4.6° and 26.6° corresponded to the (100) and (001) planes of TP1C, indicating that TP1C was successfully prepared with high degree of crystallinity. In the hybrid sample, the PXRD diffraction peaks of both TP1C and WS_2 can be observed, and the smaller peak intensity of WS_2 may be due to its low content.

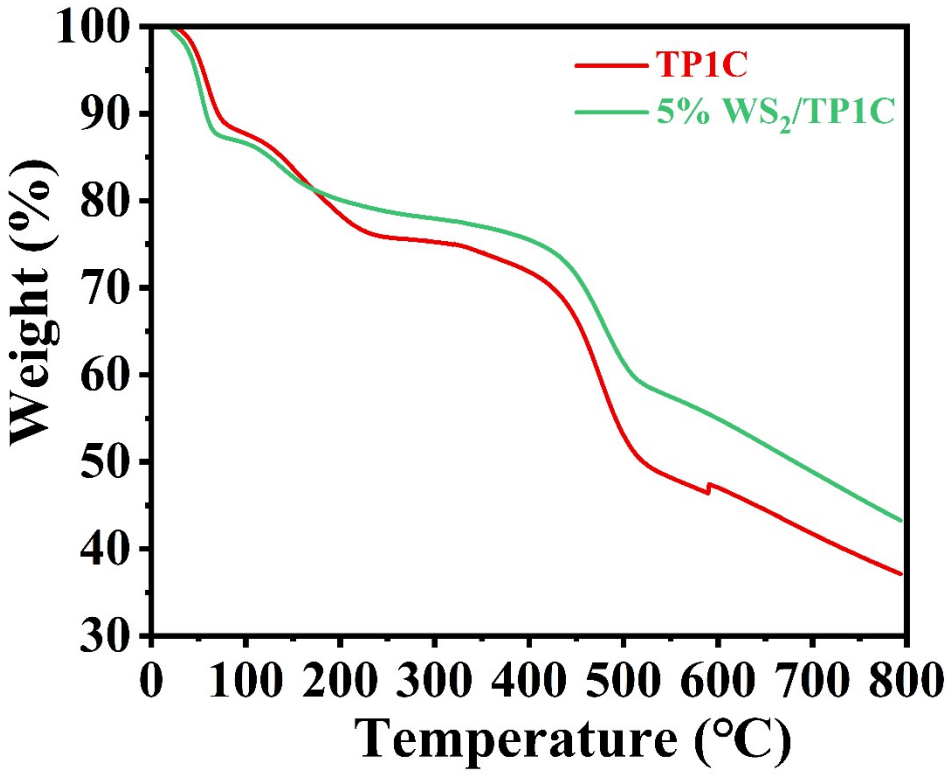

Fig. S6. The TG patterns of prepared samples. As shown in Fig. S6, the weight of prepared samples decreased as temperature increased. The weight loss before 200 °C primarily resulted from the evaporation of water or solvent on the surface or within the pores of COFs. The decomposition temperatures of bare COFs and WS_2/TP1C hybrid material were about 450 and 430 °C, respectively, indicating their excellent thermal stability.

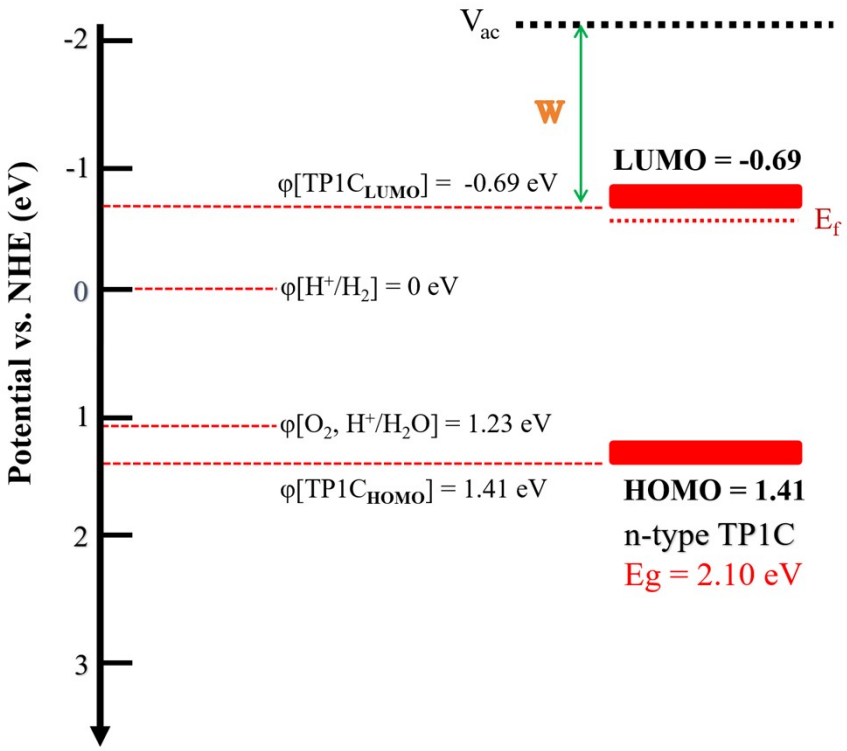

Fig. S7. Schematic energy-band image for TP1C (V_{ac}, HOMO, LUMO, E_f and W refer to vacuum level, Highest Occupied Molecular Orbit, Lowest Unoccupied Molecular Orbit, Fermi level, Work function, respectively).

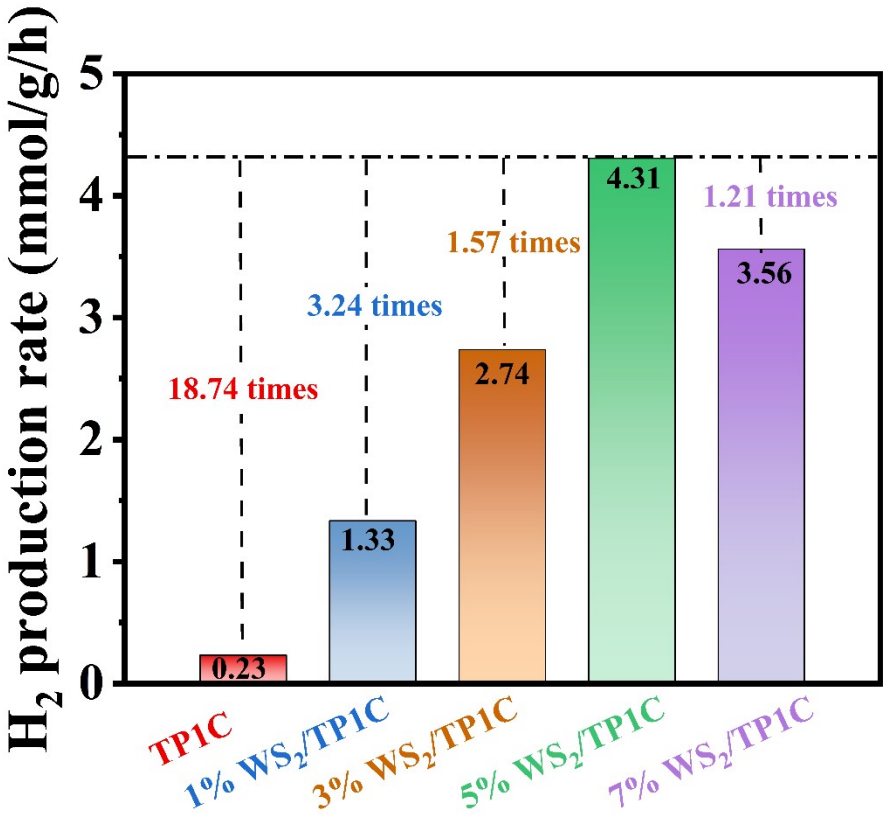

Fig. S8. Photocatalytic hydrogen evolution rate of synthesized products. As shown in Fig.S8, since WS_2 nanosheets promoted photogenerated charge transfer, 5% WS_2/TP1C exhibited optimal photocatalytic activity, which was about 18.74 times higher over that of pure COFs.

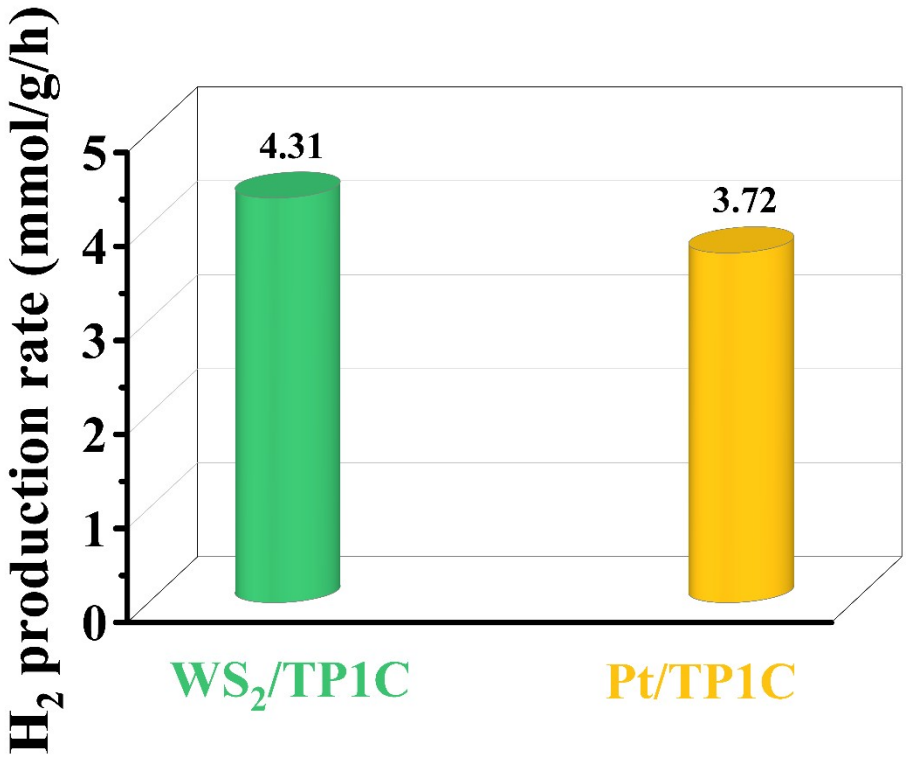

Fig. S9. Photocatalytic hydrogen evolution activity of WS_2/TP1C and Pt/TP1C. As depicted in Fig. S9, WS_2/TP1C exhibited higher photocatalytic hydrogen production rate as compared to Pt/TP1C, indicating superiority of two-dimensional co-catalysts.

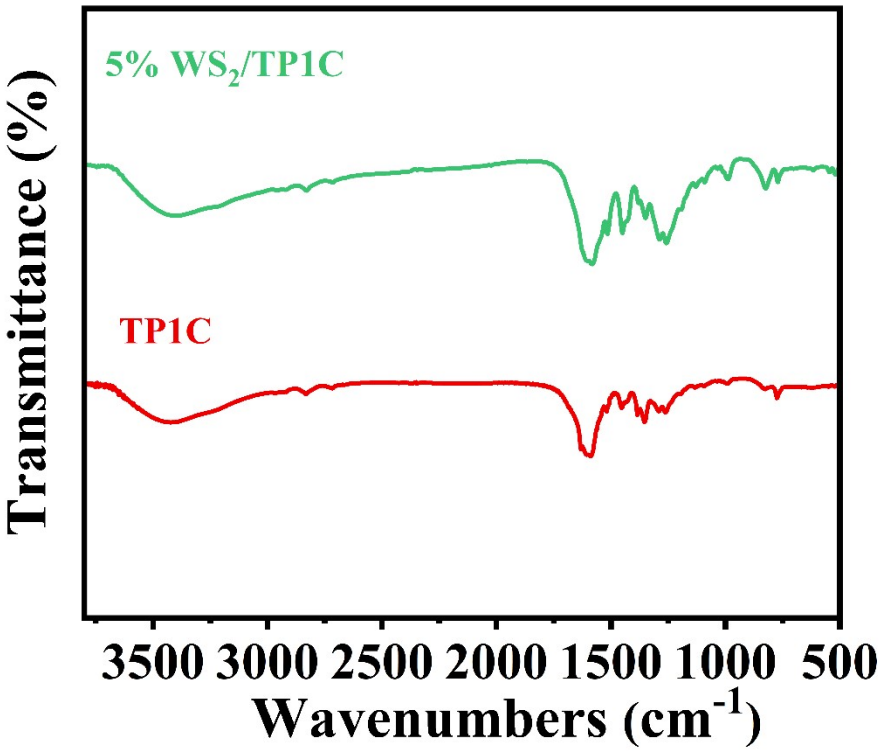

Fig. S10. Fourier-transform infrared (FT-IR) spectra of TP1C and 5% WS_2/TP1C. As shown in Fig.S10, the broad spectral range between 3000 and 3700 cm^{-1} can be ascribed to the stretching vibrations of -OH groups. The prominent peaks observed at approximately 1616 and 1451 cm^{-1} corresponded to the stretching vibrations of C=O and C=C bonds, respectively. Furthermore, the band detected around 1255 cm^{-1} was likely indicative of the stretching vibration of C-N bonds.[4]

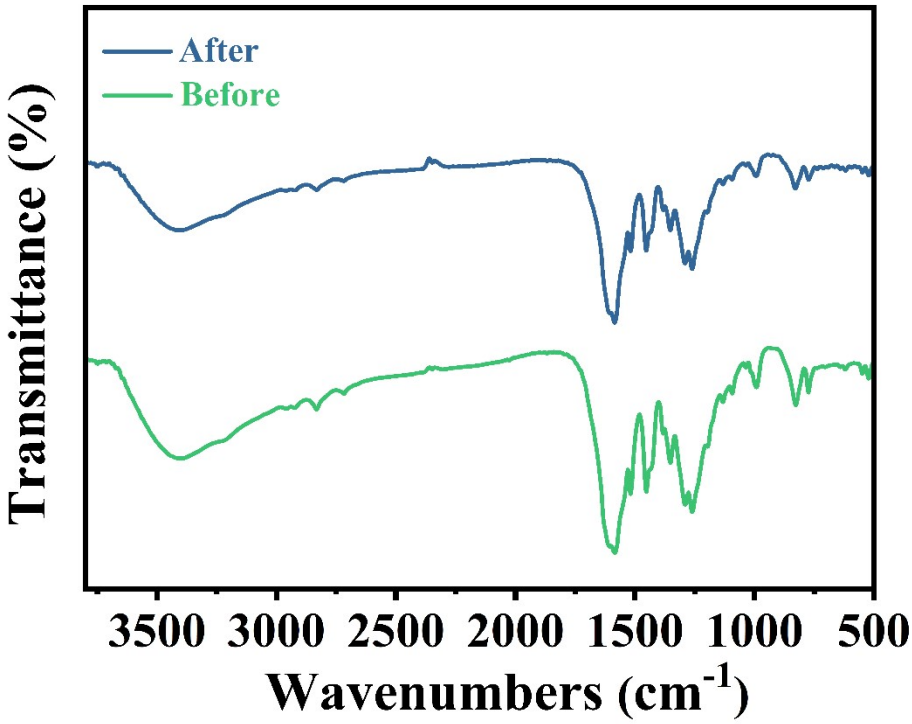

Fig. S11. Infrared spectra of 5% WS_2/TP1C before and after the photocatalytic reaction.

As illustrated in Fig. S11, the Fourier-transform infrared (FT-IR) test was imposed on 5% WS_2/TP1C after photocatalytic reaction, and the peak positions were almost consistent with those before the reaction, further proving that the prepared material possessed good durability.

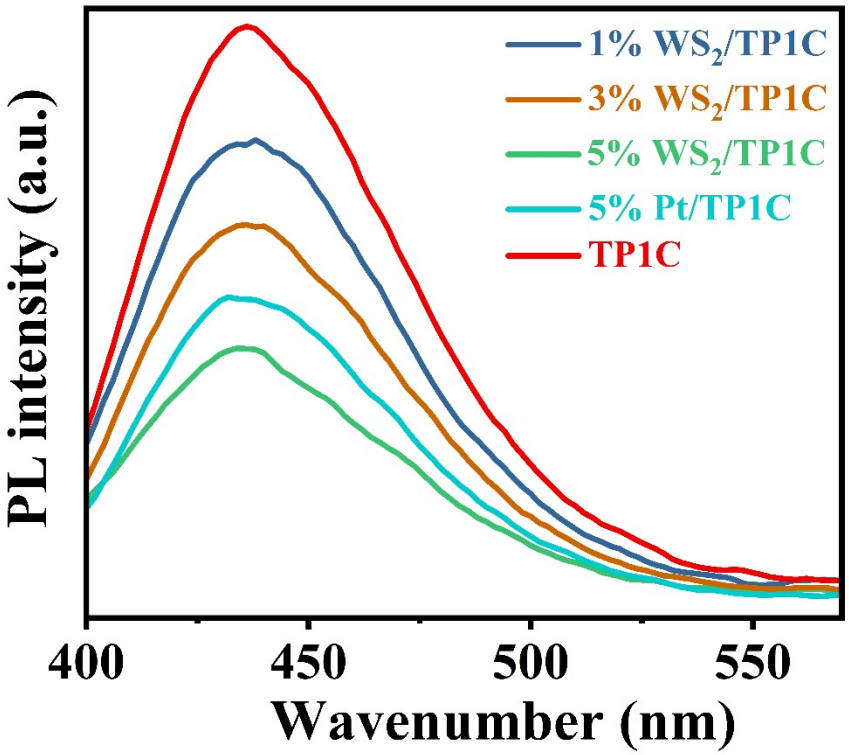

Fig. S12. The photoluminescence (PL) spectra of prepared samples. As displayed in Fig. S12, 5% WS_2/TP1C exhibited lower fluorescence intensity as compared to bare COFs and 5% Pt/TP1C due to its higher charge separation efficiency.

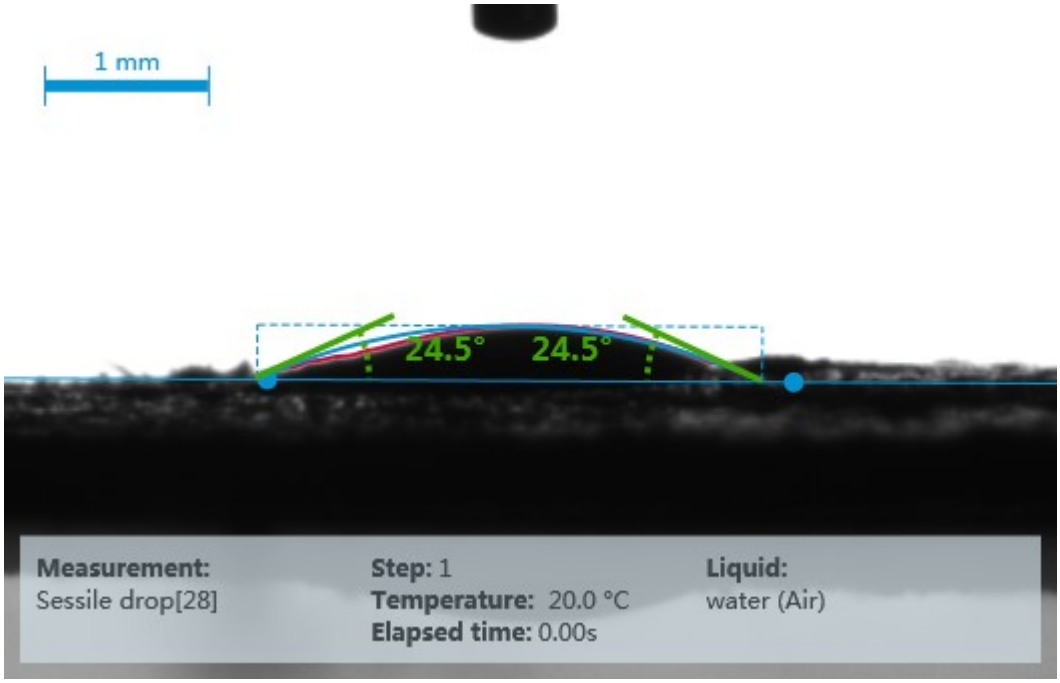

Fig. S13. The water contact angle of TP1C. As displayed in Fig. S13, the water contact angle measurements demonstrated a certain degree of hydrophilicity of pure TP1C.

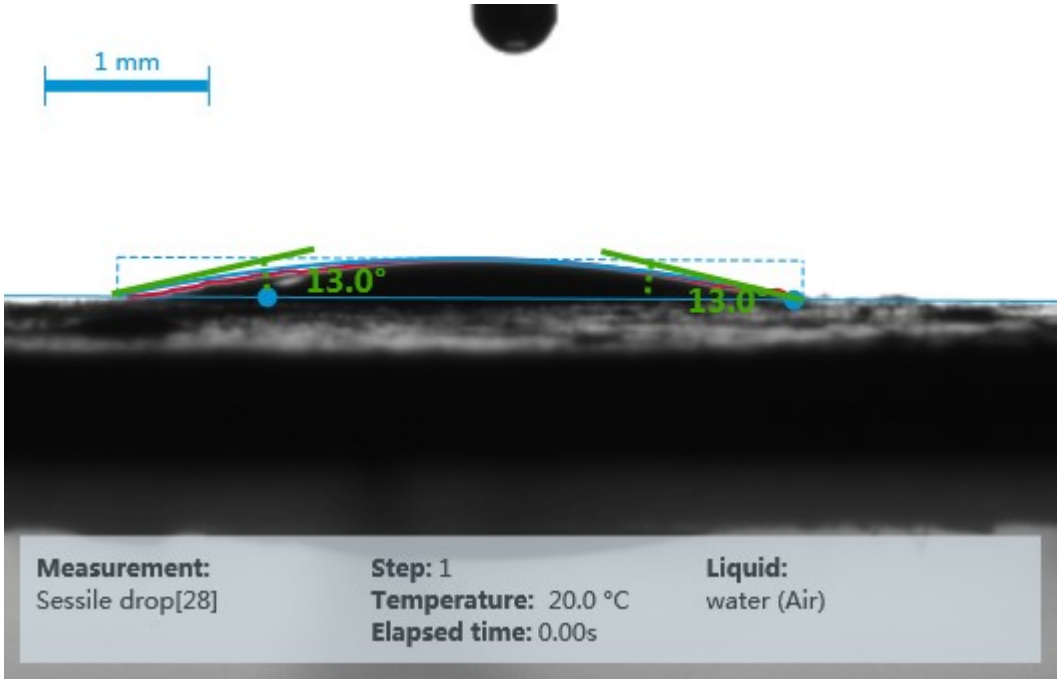

Fig. S14. The water contact angle of 5% WS_2/TP1C. As depiced in Fig. S14, 5% WS_2/TP1C owned the smaller water contact angle, proving its stronger hydrophilicity.

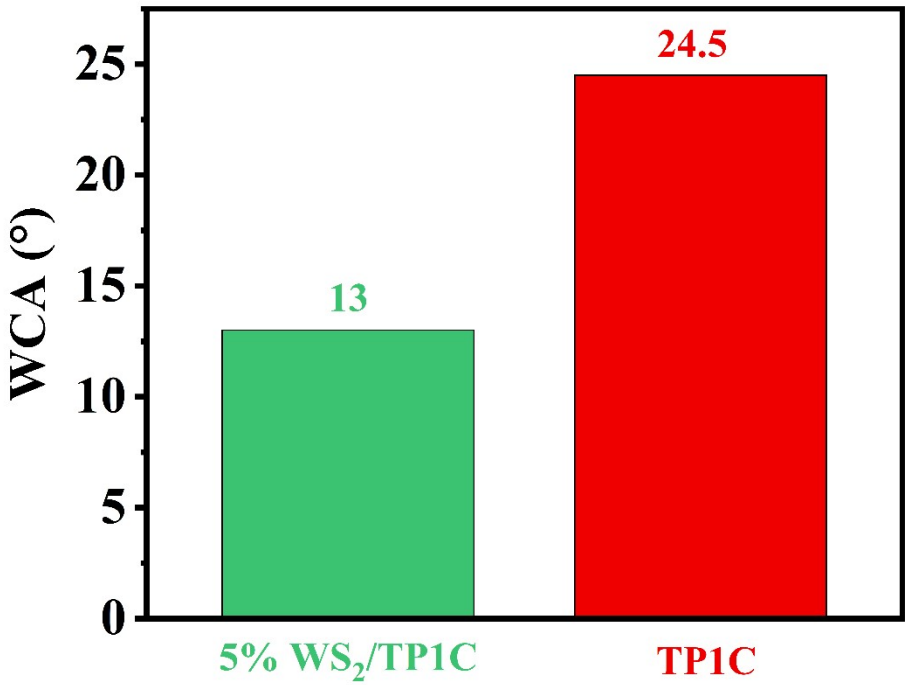

Fig. S15. The water contact angles of TP1C and 5% WS_2/TP1C. It was evident that the WS_2/TP1C hybrid sample with smaller WCA demonstrated notably higher hydrophilicity, indicating the potential for improved substrate enrichment and enhanced facilitation of photocatalytic activity for water splitting.

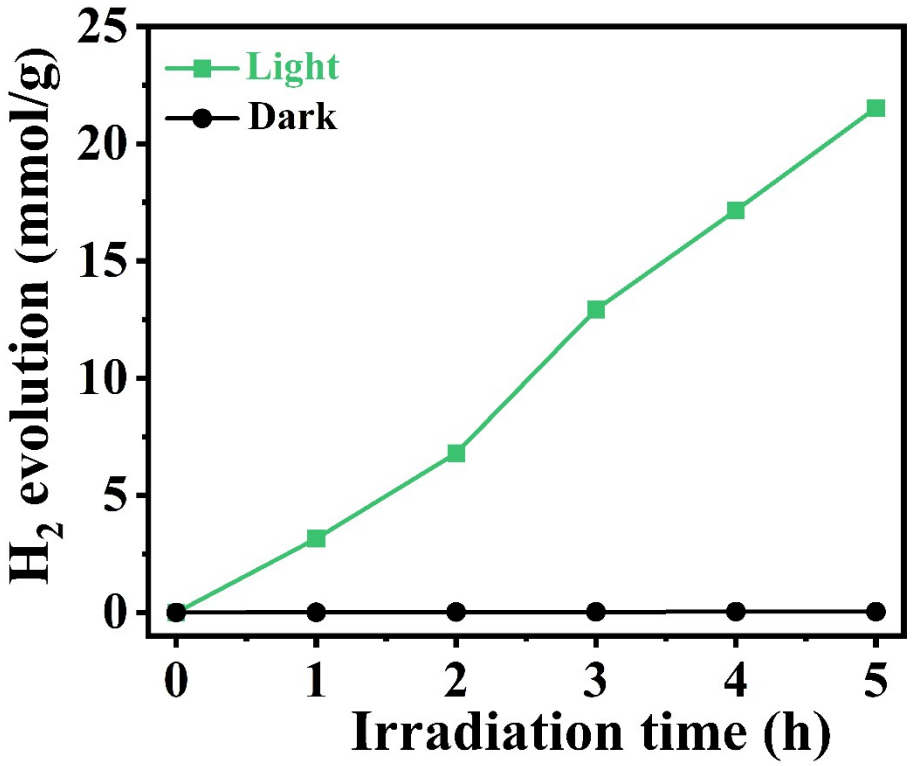

Fig. S16. The photocatalytic H_2 production rate of 5% WS_2/TP1C under dark and light irradiation. As shown in Fig. S16, the 5% WS_2/TP1C hybrid material exhibited no H_2 production under dark conditions.

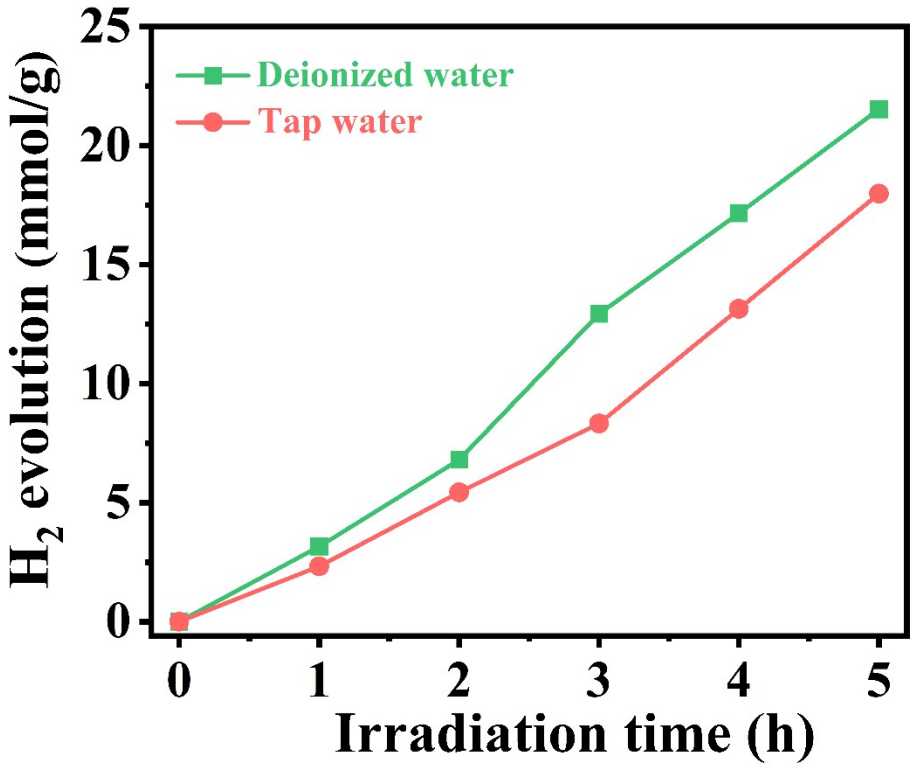

Fig. S17. Photocatalytic activity of 5% WS_2/TP1C in different water matrices. As depicted in Fig. S17, due to the effect of impurity ions, the photocatalytic activity of 5% WS_2/TP1C in tap water displayed a slight decreasing trend compared to that in deionized water, proving its potential for practical application.

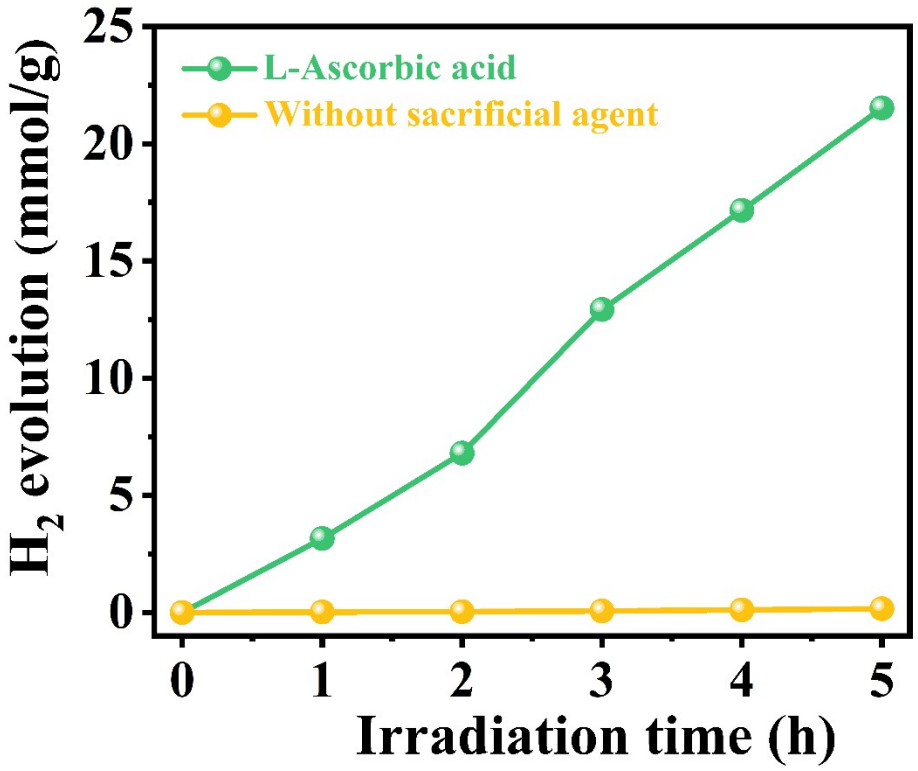

Fig. S18. The photocatalytic activity of 5% WS_2/TP1C without sacrificial agent or with L-Ascorbic acid as sacrificial agent. Obviously, the 5% WS_2/TP1C hybrid material exhibited negligible photocatalytic activity without any sacrificial agents due to severe electron-hole pair recombination issues (Fig. S18). Thus, L-Ascorbic acid, as a hole scavenger, plays a great role in enhancing the photocatalytic performance of WS_2/TP1C composites.

Table S1. The lifetime of TP1C and 5% WS_2/TP1C in time-resolved PL test

Sample	τ_1 (ns)	B_1	τ_2 (ns)	B_2	τ_{av} (ns)
TP1C	1.1112	760.0814	5.8154	50.6238	2.33
5% WS_2/TP1C	0.8288	772.2839	4.9470	92.8563	2.55

Table S2. Summary of previous reported photocatalysts with co-catalysis

Sample	Light	Sacrificial agent	Cocatalyst	H_2 evolution rate ($\mu mol \cdot g^{-1} \cdot h^{-1}$)	Ref
5% WS_2/TP1C	λ ≥ 420 nm	L-Ascorbic acid	-	4305	This work
CdS-COF	λ ≥ 420 nm	Lactic acid	Pt	3678	5
Tp-Pa-CN	λ ≥ 420 nm	Sodium ascorbate	Pt	1800	6
N3-COF	λ ≥ 420 nm	TEOA	Pt	1703	7
TZ-COF-4	λ ≥ 420 nm	L-Ascorbic acid	Pt	4296	8
TFPT-COF	λ ≥ 420 nm	Sodium ascorbate	Pt	1970	9
COF-BPDA	λ ≥ 420 nm	L-Ascorbic acid	Pt	3230	10
TAB-TFP-COF	λ ≥ 420 nm	L-Ascorbic acid	Pt	1140	11
15N-CNU	λ ≥ 420 nm	TEOA	Pt	2180	12
Co/Zn-Salen-COF	λ ≥ 420 nm	L-Ascorbic acid	-	1378	13
FL-CTF-2	λ ≥ 420 nm	TEOA	Pt	1527	14
Cl-ECF	λ ≥ 420 nm	TEOA	Pt	1296	15
CTF-N	λ ≥ 420 nm	TEOA	Pt	538	16
Pt_1@TpPa-1	λ ≥ 420 nm	Sodium ascorbate	-	719	17
$Ni_{12}P_5$/TpPa-1-COF	λ ≥ 420 nm	L-Ascorbic acid	-	3160	18
PyTA-BC-Ph	λ ≥ 420 nm	L-Ascorbic acid	Pt	2763	19
TPCNNS-2	λ ≥ 420 nm	Sodium ascorbate	Pt	1153	20
$Ni(OH)_2$-2.5%/COF	λ ≥ 420 nm	Sodium ascorbate	-	1895.99	21
ZnPor-DETH-COF	λ > 400 nm	TEOA	Pt	413	22
Py-1P-Ir	460 nm LED light	HCOONa	-	1358	23
CuCo@C/g-C_3N_4	λ ≥ 420 nm	TEOA	-	2120	24

References

1 Y. Lei, K. H. Ng, Y. Zhu, Y. Zhang, Z. Li, S. Xu, J. Huang, J. Hu, Z. Chen, W. Cai, Y. Lai, *Chem. Eng. J.*, 2023, **452**, 139325.

2 Z. Qian, R. Zhang, H. Hu, Y. Xiao, H. Li, X. Sun, T. Ma, *Solar RRL*, 2023, **7**, 2300547.

3 C. Zhang, C. Xie, Y. Gao, X. Tao, C. Ding, F. Fan, H.-L. Jiang, *Angew. Chem. Int. Ed.*, 2022, **61**, e202204108.

4 W. Weng, J. Guo, *Nat. Commun.*, 2022, **13**, 5768.

5 J. Thote, H. B. Aiyappa, A. Deshpande, D. Díaz Díaz, S. Kurungot, R. Banerjee, *Chem. Eur. J.*, 2014, **20**, 15961-15965.

6 L. Wang, L. Zhang, B. Lin, Y. Zheng, J. Chen, Y. Zheng, B. Gao, J. Long, Y. Chen, *Small*, 2021, **17**, 2101017.

7 V. S. Vyas, F. Haase, L. Stegbauer, G. Savasci, F. Podjaski, C. Ochsenfeld, B. V. Lotsch, *Nat. Commun.*, 2015, **6**, 8508.

8 K. Wang, Z. Jia, Y. Bai, X. Wang, S. E. Hodgkiss, L. Chen, S. Y. Chong, X. Wang, H. Yang, Y. Xu, F. Feng, J. W. Ward, A. I. Cooper, *J. Am. Chem. Soc.*, 2020, **142**, 11131-11138.

9 L. Stegbauer, K. Schwinghammer, B. V. Lotsch, *Chem. Sci.*, 2014, **5**, 2789-2793.

10 S. Bi, F. Meng, D. Wu, F. Zhang, *J. Am. Chem. Soc.*, 2022, **144**, 3653-3659.

11 X. Wu, M. Zhang, Y. Xia, C. Ru, P. Chen, H. Zhao, L. Zhou, C. Gong, J. Wu, X. Pan, *J. Mater. Chem. A*, 2022, **10**, 17691-17698.

12 J.-P. Zou, L.-C. Wang, J. Luo, Y.-C. Nie, Q.-J. Xing, X.-B. Luo, H.-M. Du, S.-L. Luo, S. L. Suib, *Appl. Catal. B: Environ.*, 2016, **193**, 103-109.

13 W. Zhou, Q.-W. Deng, H.-J. He, L. Yang, T.-Y. Liu, X. Wang, D.-Y. Zheng, Z.-B. Dai, L. Sun, C. Liu, H. Wu, Z. Li, W.-Q. Deng, *Angew. Chem. Int. Ed.*, 2023, **62**, e202214143.

14 L. Li, Y. Zhu, N. Gong, W. Zhang, W. Peng, Y. Li, F. Zhang, X. Fan, *Int. J. Hydrogen Energy*, 2020, **45**, 2689-2698.

15 S. Li, M.-F. Wu, T. Guo, L.-L. Zheng, D. Wang, Y. Mu, Q.-J. Xing, J.-P. Zou, *Appl. Catal. B: Environ.*, 2020, **272**, 118989.

16 L. Guo, Y. Niu, H. Xu, Q. Li, S. Razzaque, Q. Huang, S. Jin, B. Tan, *J. Mater. Chem. A*, 2018, **6**, 19775-19781.

17 P. Dong, Y. Wang, A. Zhang, T. Cheng, X. Xi, J. Zhang, *ACS Catal.*, 2021, **11**, 13266-13279.

18 K. Zhang, X. Sun, H. Hu, G. Yan, A. Qin, Y. Ma, H. Huang, T. Ma, *Small*, 2023, **19**, 2304674.

19 A. F. M. El-Mahdy, A. M. Elewa, S.-W. Huang, H.-H. Chou, S.-W. Kuo, *Adv. Opt. Mater.*, 2020, **8**, 2000641.

20 P. Dong, A. Zhang, T. Cheng, J. Pan, J. Song, L. Zhang, R. Guan, X. Xi, J. Zhang, *Chin. J. Catal.*, 2022, **43**, 2592-2605.

21 H. Dong, X.-B. Meng, X. Zhang, H.-L. Tang, J.-W. Liu, J.-H. Wang, J.-Z. Wei, F.-M. Zhang, L.-L. Bai, X.-J. Sun, *Chem. Eng. J.*, 2020, **379**, 122342.

22 R. Chen, Y. Wang, Y. Ma, A. Mal, X.-Y. Gao, L. Gao, L. Qiao, X.-B. Li, L.-Z. Wu, C. Wang, *Nat. Commun.*, 2021, **12**, 1354.

23 J. Hu, H. Mehrabi, Y.-S. Meng, M. Taylor, J.-H. Zhan, Q. Yan, M. Benamara, R. H. Coridan, H. Beyzavi, *Chem. Sci.*, 2021, **12**, 7930-7936.

24 S. Chen, Z. Yang, J. Chen, J. Liao, S. Yang, F. Peng, L.-X. Ding, G. Yang, S. Zhang, Y. Fang, *Chem. Eng. J.*, 2022, **434**, 134673.